Use of radiolabeled hyaluronic acid for preclinical assessment of inflammatory injury and acute respiratory distress syndrome

Fangyuan Zhao [a,d], Christy J. Barber [a], Saad Sammani [b], Li Wan [a], Brian W. Miller [a,c], Lars R. Furenlid [a,c], Zheng Li [e], Deepa B. Gotur [f], Roberto Barrios [g], James M. Woolfenden [a], Diego R. Martin [e], Zhonglin Liu [a,e,*,1]

[a] Department of Medical Imaging, University of Arizona, Tucson, AZ, United States of America
[b] Department of Medicine, University of Arizona, Tucson, AZ, United States of America
[c] College of Optical Sciences, University of Arizona, Tucson, AZ, United States of America
[d] Food Science and Engineering College, Qingdao Agricultural University, China
[e] Department of Radiology, Houston Methodist Hospital, Houston, TX, United States of America
[f] Department of Medicine, Houston Methodist Hospital, Houston, TX, United States of America
[g] Department of Pathology, Houston Methodist Hospital, Houston, TX, United States of America

ARTICLE INFO

Keywords:
Hyaluronic acid (HA)
Radiolabeled-HA
Inflammatory injury
Lung
ARDS
Imaging

ABSTRACT

Acute respiratory distress syndrome (ARDS) is accompanied by a dramatic increase in lung hyaluronic acid (HA), leading to a dose-dependent reduction of pulmonary oxygenation. This pattern is associated with severe infections, such as COVID-19, and other important lung injury etiologies. HA actively participates in molecular pathways involved in the cytokine storm of COVID-19-induced ARDS. The objective of this study was to evaluate an imaging approach of radiolabeled HA for assessment of dysregulated HA deposition in mouse models with skin inflammation and lipopolysaccharide (LPS)-induced ARDS using a novel portable intensified Quantum Imaging Detector (iQID) gamma camera system.

Methods: HA of 10 kDa molecular weight (HA10) was radiolabeled with ^{125}I and ^{99m}Tc respectively to produce [^{125}I]I-HA10 and [^{99m}Tc]Tc-HA10, followed by comparative studies on stability, in vivo biodistribution, and uptake at inflammatory skin sites in mice with 12-O-tetradecanoylphorbol-13-acetate (TPA)-inflamed ears. [^{99m}Tc]Tc-HA10 was used for iQID in vivo dynamic imaging of mice with ARDS induced by intratracheal instillation of LPS.

Results: [^{99m}Tc]Tc-HA10 and [^{125}I]I-HA10 had similar biodistribution and localization at inflammatory sites. [^{99m}Tc]Tc-HA10 was shown to be feasible in measuring skin injury and monitoring skin wound healing. [^{99m}Tc]Tc-HA10 dynamic pulmonary images yielded good visualization of radioactive uptake in the lungs. There was significantly increased lung uptake and slower lung washout in mice with LPS-induced ARDS than in control mice. Postmortem biodistribution measurement of [^{99m}Tc]TcHA10 (%ID/g) was 11.0 ± 3.9 vs. 1.3 ± 0.3 in the ARDS mice (n = 6) and controls (n = 6) ($P < 0.001$), consistent with upregulated HA expression as determined by enzyme-linked immunosorbent assay (ELISA) and immunohistochemistry (IHC) staining.

Conclusions: [^{99m}Tc]Tc-HA10 is promising as a biomarker for evaluating HA dysregulation that contributes to pulmonary injury in ARDS. Rapid iQID imaging of [^{99m}Tc]Tc-HA10 clearance from injured lungs may provide a functional template for timely assessment and quantitative monitoring of pulmonary pathophysiology and intervention in ARDS.

1. Introduction

Acute respiratory distress syndrome (ARDS) is the leading cause of death in critical care patients [1–3]. The clinical disorders associated with the development of ARDS include all types of lung injuries resulting from sepsis, viral infections like coronavirus disease 2019 (COVID-19), pneumonia, trauma, burns, aspiration of gastric contents, and acute pancreatitis [4–8]. ARDS is characterized by increased vascular permeability, pulmonary edema, severe arterial hypoxemia, and impaired carbon dioxide excretion. Lung imaging is a fundamental tool for assessing the morphological and mechanistic features of ARDS and plays a crucial role in diagnosing and managing ARDS [1–3,9]. In recent years, inflammation and molecular imaging have provided new insights into ARDS pathophysiology and may lead to new approaches to managing ARDS patients [9,10].

Hyaluronic acid (HA) or hyaluronan, a polysaccharide synthesized by a class of integral membrane hyaluronan synthases of stromal cells and deposited in the extracellular matrix (ECM), is closely involved with the pathophysiology of ARDS [5,11–13]. Following lung injury, aberrant HA production from mast cells, epithelial cells, endothelial cells, and fibroblasts leads to excess HA accumulation in the airway lumen, thickened perialveolar interstitium, and alveolar obstruction, thereby reducing lung compliance and ventilation [2,14–17]. Small HA fragments generated by multiple mechanisms in the exudative phase of ARDS are actively involved in signaling pathways of the cytokine release syndrome (CRS) or so-called cytokine storm that manifest systemic immune-mediated processes, fever, and multi-organ dysfunction [5,7,11,12,18,19]. The small HA fragments and oligosaccharides serve as Toll-like receptors (TLRs) agonists to initiate inflammatory cascades that promote inflammatory cell recruitment and activation. In addition to the TLRs pathway, HA fragments play an essential role in downstream inflammatory signaling via the receptor for HA-mediated motility (RHAMM), which is expressed minimally or not in normal tissues, in response to robust pulmonary inflammation and ARDS [14,20–23]. HA is also a powerful water-binding substance that contributes to the interstitial and alveolar edema in ARDS, leading to histologic findings of "hyaline membranes" observed in COVID-19 victims [24], for example. The COVID-19 global pandemic has created a need for improved diagnostics. An imaging strategy for noninvasive measurement of HA kinetics, from synthesis to clearance, and validation of use for monitoring ARDS may be invaluable for clinical applications.

HA fragments can be labeled with radioisotopes suitable for SPECT (^{123}I, ^{99m}Tc, and ^{111}In) and PET (^{124}I) imaging [25–27]. HA's size significantly influences receptor binding, cell uptake, and tissue distribution. HA fragments of low molecular weight (generally <200 kDa) are considered more biologically active and proinflammatory than high molecular weight forms, particularly if the molecular size is <100 kDa [2,5,16,28,29]. Especially, HA fragments with 10 kDa molecular weight, hereinafter called HA10, possesses notable inflammatory effects with immunostimulatory and pro-angiogenic activity in human cells. In this study, we radiolabeled HA10 with ^{125}I and ^{99m}Tc to produce [^{125}I]I-HA10 and [^{99m}Tc]Tc-HA10 for experimental assessment of inflammatory injury and ARDS. Typically, ^{125}I-radioiodinated molecules are used for in vitro and ex vivo characterization of biodistribution, but significant absorption of emissions by body tissues and long half-life make it impractical for in vivo imaging studies using a conventional gamma camera or SPECT system. ^{99m}Tc is widely used for clinical imaging in nuclear medicine and has the advantages of low cost, good emission energy, and half-life. Using a newly developed intensified Quantum Imaging Detector (iQID) camera [30,31], which has high sensitivity at low and medium gamma-ray energies and is suitable for imaging the low-energy emissions from ^{125}I and moderate-energy emissions from ^{99m}Tc, we compared the distribution of [^{125}I]I-HA10 and [^{99m}Tc]Tc-HA10 in mice to see if they showed equivalent biological behavior for assessment of tissue inflammatory responses. Accordingly, an established mouse-ear inflammation model was used to perform the comparative evaluation of inflammatory skin injury with [^{125}I]I-HA10 and [^{99m}Tc]Tc-HA10 imaging. Subsequently, [^{99m}Tc]Tc-HA10 imaging was characterized for assessing attenuation of inflammation-induced skin injury in the inflamed mouse-ear model by administration of highly size-specific HA solution with 35 kDa molecular weight, starting now called HA35. iQID dynamic imaging with [^{99m}Tc]Tc-HA10 was used in a mouse model with lipopolysaccharide (LPS)-induced ARDS to elucidate dysregulated HA kinetics associated with the pathophysiology of inflammatory lung diseases.

2. Materials and methods

2.1. Materials

HA10 was purchased from Lifecore Biomedical (Chaska, Minnesota). Highly purified HA35 fragment preparations were obtained from Shaoxing HH Technology, Inc. (Shaoxing, China). Cyanogen bromide (CNBr), DL-tyrosine (Tyr), tyramine (TA), sodium glucoheptonate (GH), stannous chloride dihydrate, 12-O-tetradecanoylphorbol-13-acetate (TPA), LPS from *Escherichia coli* 0127:B8 and other chemicals were purchased from Millipore Sigma (St. Louis, MO). ^{125}I was obtained from PerkinElmer (Boston, MA). ^{99m}Tc pertechnetate (^{99m}TcO$_4^-$) was provided by Cardinal Health (Tucson, AZ). Pierce Iodination tubes precoated at the bottom with 50 μg Pierce Iodination Reagent were obtained from Thermo Fisher Scientific™ (Waltham, MA).

2.2. Iodination of HA10 with ^{125}I

HA10 was activated with CNBr and then iodinated as described previously [32–34]. We first radioiodinated HA10 with ^{125}I via Tyr substitution and obtained [^{125}I]I-Tyr-HA10. The iodination protocol via Tyr substitution was compared to an alternative protocol, in which a reactive aromatic Tyr derivative, TA, was attached to the HA10 molecule and yielded [^{125}I]I-TA-HA10. In brief, 10 mg of HA10 in 1 mL of water is activated by adding 200 μL CNBr (40 mg/mL). The mixture is adjusted to pH 11 and maintained for 5 min by adding 0.2 M NaOH. The activated HA10 is separated from the reaction mixture on a small Sephadex G25 (PD10) column equilibrated with 0.2 M borate buffer pH 8.0. CNBr-activated HA10 molecules were incubated overnight with 0.5–1.0 mg Tyr or TA. Sephadex G-25 column was used to separate Tyr- or TA-bound HA10 (Tyr-HA10 and TA-HA10) from unbound Tyr/TA. Iodination was carried out by incubating 250 μL modified HA10 (100 μg) with 1.0 mCi ^{125}I in the Pierce Pre-Coated Iodination Tubes for 15 min at room temperature. The tubes were gently agitated every minute during incubation. Reaction mixtures were removed from the reaction tubes to terminate the iodide oxidation and then loaded to PD10 columns for purification. An illustration of HA10 and ^{125}I-iodinated HA10 molecular structure and iodination protocol is shown in Fig. 1A. Radioiodination efficiency (radiochemical purity, RCP) was determined by instant thin layer chromatography (ITLC) on glass-fiber chromatography paper impregnated with silica gel (Agilent Technologies, Santa Clara, CA) using a 50/50 mixture of 0.1 M sodium citrate solution at pH 5 and acetonitrile as the mobile phase [25]. The retention factor (Rf) of ^{125}I-iodinated HA10 is 1.0. Fractionally collected [^{125}I]I-Tyr-HA10 and [^{125}I]I-TA-HA10 with RCP >98 % were stored at 2–8 °C for use within two weeks.

2.3. ^{99m}Tc-labeling of HA10

Labeling of HA10 with ^{99m}Tc was based on a straightforward procedure described previously, in which technetium was reduced to Tc(V) as [TcOCl$_4$]$^-$ by stannous chloride (SnCl$_2$), bound to the carboxyl group of HA10, and formed a stable compound of radiolabeled HA10, [^{99m}Tc]Tc-HA10 [25–27]. ^{99m}Tc-labeling of HA10 was comparatively performed with and without GH as an exchange agent to chelate tin-reduced ^{99m}TcO$_4^-$ to HA10. Physiological saline solution and 0.1 N
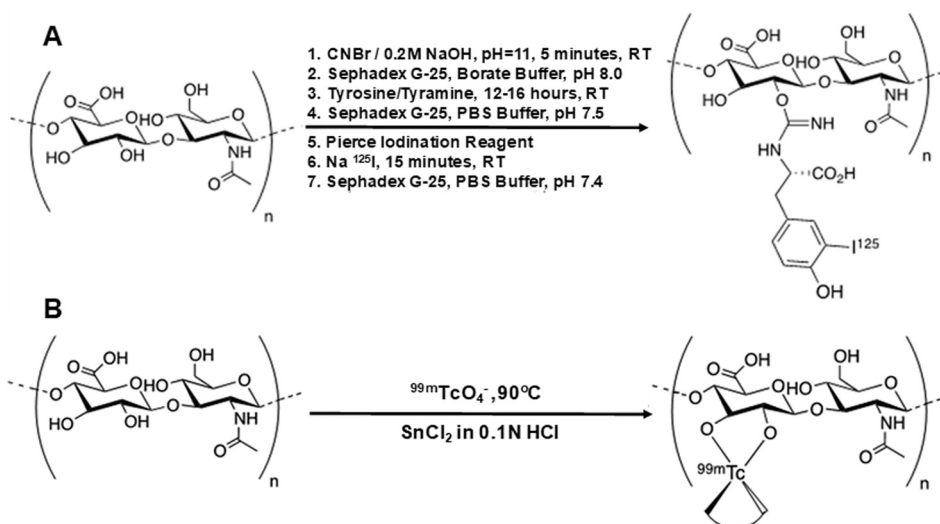
Fig. 1. Illustrations of radiolabeling HA with ^{125}I and ^{99m}Tc to produce [^{125}I]I-TA-HA10 (A) and [^{99m}Tc]Tc-HA10 (B).

HCl were prepared and bubbled by N_2 for 15 min. In the protocol using an exchange agent, 1.0 mg of HA10 in 20 μL water was added to a mixture of 200 μL of ^{99m}TcO$_4^-$ (~10 mCi) and 50 μL of GH solution (20 mg/mL) prepared in de-oxygenated saline followed by addition of 5 μL SnCl$_2$ (2 mg/mL) in de-oxygenated 0.1 N HCl. In the direct labeling protocol, 5 μL SnCl$_2$ (2 mg/mL) was added to a mixture of 1.0 mg HA10 in 20 μL water and 250 μL of ^{99m}TcO$_4^-$ (~10 mCi) in saline. The reaction mixtures were incubated at 80 °C for 90 min. Size exclusion-high-performance liquid chromatography (SEC-HPLC) analysis was performed to measure radiolabeling yield, and RCP of each ^{99m}Tc-labeled product using a Shodex KW 802.5 column (7.8 × 300 mm, 5 μm particle size) (Thomson Instrument Co., Oceanside, CA) equilibrated and eluted with phosphate-buffered saline (PBS) at pH 7.4 at a flow rate of 0.8 mL/min. The SEC-HPLC analyses were carried out using a Waters Breeze system (Waters Technologies Corp., Milford, MA) equipped with a Waters 1525 Binary HPLC Pump and a Waters 2489 dual absorbance detector (280 nm) in line with a Flow-Count™ Radio HPLC Flow Through Detector (Bioscan Inc., Washington, DC). An illustration of HA and ^{99m}Tc-labeled HA10 molecular structure with the direct labeling protocol is shown in Fig. 1B.

2.4. Stability of radiolabeled HA10

After purification, the stability of radiolabeled products was determined in fresh rat serum at 37 °C as previously described with slight modifications [25–27,34]. A solution of 50 μL ^{125}I-iodinated HA10 (~0.14 mg/mL) or ^{99m}Tc-labeled HA10 (~1.0 mg/mL) in PBS (pH 7.4) was incubated with 50 μL serum. The RCP of the mixture was selectively analyzed for 5 h after mixing using ITLC for ^{125}I-iodinated HA10 and SEC-HPLC for ^{99m}Tc-labeled HA10.

2.5. Novel small-animal iQID camera

iQID camera (Fig. 2) was used to image the whole-body distribution of the radiolabeled HA10 in healthy mice and mouse models with lung injury. The iQID system developed at the University of Arizona uses CCD or CMOS sensors to image scintillation light amplified with an image intensifier. This compact small-animal imaging system provides detection of photon (or particle) emissions with high spatial resolution and high sensitivity at both low and medium gamma energies, enabling imaging of both ^{125}I- and ^{99m}Tc-labeled radiotracers [30,31]. It also provides high temporal resolution for dynamic imaging and radiotracer kinetic analysis.
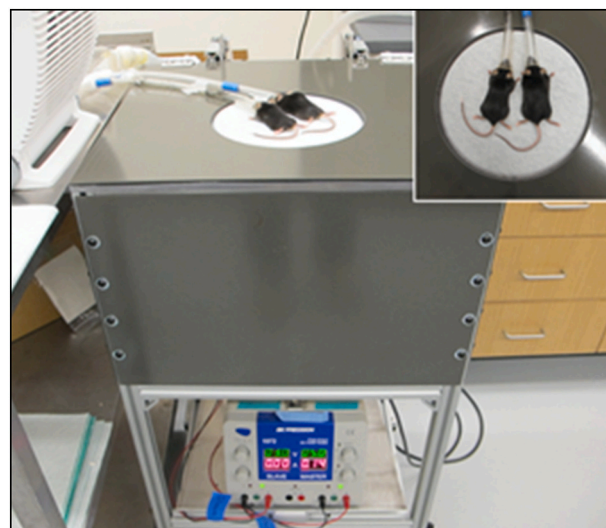

Fig. 2. iQID scintigraphic system used to acquire images of radiolabeled HA10 in mouse models. Inset: closeup of mice during the imaging session.

2.6. Imaging of [^{125}I]I-TA-HA10 and [^{99m}Tc]Tc-HA10 biodistribution in healthy mice

Based on stability measurements, [^{125}I]I-Tyr-HA10 was excluded from subsequent in vivo studies due to its lower stability than [^{125}I]I-TA-HA10. Similarly, [^{99m}Tc]Tc-HA10 product resulting from the GH exchange protocol was not included in the in vivo studies because of lower stability than [^{99m}Tc]Tc-HA10 generated using the direct labeling protocol.

Using the iQID camera, whole-body images of [^{125}I]I-TA-HA10 and [^{99m}Tc]Tc-HA10 were acquired in healthy sex-matched C57BL/6 J mice (Charles River Laboratories, Wilmington, Mass) at age 6–8 weeks (n = 5 for each) to reveal the tracer biodistribution. [^{125}I]I-TA-HA10 (150–200 μCi) or [^{99m}Tc]Tc-HA10 (0.8–1.2 mCi) obtained from the direct labeling protocol was intravenously injected in the mice and imaged for 15 min at 180 min post-injection before the animals were euthanized. Blood and major organs were harvested for ex vivo radioactive measurements. Biodistribution results in the samples were calculated and expressed as the percent injected dose per gram of tissue (%ID/g).

2.7. Comparison of [125I]I-TA-HA10 and [99mTc]Tc-HA10 uptake at ear skin injury site

A mouse model of ear edema was adopted to evaluate and compare the capability of [125I]I-TA-HA10 and [99mTc]Tc-HA10 for the localization of inflammatory processes [35,36]. The mouse ear edema was induced in ICR mice, a strain of albino mice widely used in infection and pharmacology. Twelve age- and sex-matched mice (10–15 weeks) purchased from the Jackson Laboratory were treated by topical application of 2.0 μg TPA in 20 μL acetone to the inner and outer surface of the right ear per mouse using a micropipette. TPA treatment, which causes epidermal hyperplasia, was repeated at 24-h intervals [35–37]. The left ear was used as a control and treated with acetone, representing the carrier solvent. Four hours after i.v. injection of [125I]I-TA-HA10 (150–200 μCi) (n = 6) or [99mTc]Tc-HA10 (0.8–1.2 mCi) (n = 6), all mice were euthanized by sodium pentobarbital (Nembutal). The ears were harvested for count-based activity measurement and ex vivo autoradiography. The ears of mice that received [99mTc]Tc-HA10 were formalin-fixed and processed for hematoxylin and eosin (H&E) staining and immunohistochemistry (IHC) HA staining as described below.

2.8. Assessment of skin wound healing improvement with [99mTc]Tc-HA10

A chronic skin inflammation model, which is characterized by ear edema, increased tissue cellularity, inflammatory cell infiltration, and epidermal hyperplasia [38–40], was established to evaluate the correlation between [99mTc]Tc-HA10 uptake at the site of skin injury and wound healing improvement by the small specific-sized HA35 treatment. Ten C57BL/6 J mice received daily topical applications of 1.0 μg TPA in 20 μL acetone on the right ear for five days. The left ear received acetone as control. Before each topical application of TPA, five mice were treated by intraperitoneal injection of 1.0 mL HA35 (20 mg/mL). Five mice in another group were injected with saline instead of HA35 as controls. Ear thicknesses were measured using a digital caliper before each TPA challenge. Three hours after the last TPA or saline treatment, [99mTc]Tc-HA10 was intravenously injected. At 4 h post-injection, the mice were sacrificed, and ears were harvested for radioactive measurements and histological assays.

2.9. LPS-induced ARDS mouse model

Wild-type sex and age-matched (8–12 weeks of age) C57BL/6 J mice were anesthetized by intraperitoneal injection of ketamine (100 mg/kg) and xylazine (5 mg/kg) and then intubated with a 20-gauge angiocatheter. Lung injury was induced by intratracheal instillation of LPS (*E. coli* 0127:B8) at a 1 mg/kg dose via the 20-gauge catheter [41,42]. Control mice received instillation of the same volume of sterile saline as a carrier vehicle. The mice were recovered from anesthesia and allowed to breathe spontaneously for further experimental studies.

2.10. Characterization of ARDS mice

2.10.1. Enzyme-linked immunosorbent assay (ELISA) of lung HA content
To verify the presence and level of HA in healthy and injured lungs with LPS-induced ARDS, ELISA was used to quantify native HA expression in the lungs using the commercial Hyaluronan Quantikine® ELISA Kit (Catalog Number DHYAL0, R&D Systems) [43]. Five mice of each group that received LPS or saline treatment were euthanized at 7 h post intratracheal instillation. The lungs were immediately harvested, rinsed with PBS, and lyophilized. Tissue samples of 0.1 g taken randomly from both lungs were homogenized with a tissue homogenizer in 600 μL PBS. An equal volume of Cell Lysis Buffer 2 was added (R&D Systems®, Catalog # 895347), and tissues were lysed at room temperature for 30 min with gentle agitation. After centrifugation, supernatants were aliquoted and stored at −80 °C for a later ELISA assay to determine the

total amount of HA according to the manufacturer's protocol. Samples with 128–256-fold dilutions and standards were run in duplicates. The optical density of reactions in microplate wells was read using a microplate reader set to 450 nm. The HA levels measured in the tissue specimens were reported using the concentration of homogenated lung supernatant (ng/mL).

2.10.2. H&E and IHC staining of lungs
After sampling for ELISA, the remaining segments of the lungs in the five mice per group above were fixed in 4 % formalin for 24 h. Samples were prepared in paraffin blocks, cut at 5 μm into multiple slices, and mounted onto microscope slides for analysis. The fixed slices were stained with H&E to evaluate the overall architecture and inflammatory cell infiltration by microscopic examination. IHC HA staining of paraffin-embedded lung sections was performed using Leica Bond RXm Autostainer [44,45]. Slides were loaded onto the Leica Bond RXm, baked and deparaffinized. Heat-induced epitope retrieval was applied using tris-EDTA to the slides for 20 min at 98 °C. Endogenous peroxidase was blocked at 20 °C for 5 min with a Bond Polymer Refine kit (Leica, cat# DS9800) and then incubated with sheep polyclonal antibody against hyaluronic acid (Abcam, cat# ab53842) at a 1/300 dilution for 15 min. The secondary antibody, peroxidase-conjugated goat anti-Armenian hamster IgG (Jackson Immuno Research, cat#127-585-160), was incubated for 15 min. Color development was visualized with diaminobenzidine (DAB) chromogen of Bond Polymer Refine kit and then counterstained with hematoxylin.

Microscopic images of lung sections with H&E staining and IHC HA staining were acquired using an MVX10 microscope with a DP80 digital camera (Olympus, Tokyo, Japan). The area and intensity of HA deposition positively immunostained on lung section were quantified using SigmaScan computer software (Systat Software, Inc., San Jose, CA) in Fill Measurement Mode with an automatic threshold at ~60 %.

2.11. Imaging pulmonary deposition and clearance of [99mTc]Tc-HA10 in lungs with ARDS

We used the mouse model with LPS-induced ARDS to delineate characteristics of [99mTc]Tc-HA10 corresponding to the pulmonary inflammatory response. Sex- and age-matched C57BL/6 J mice (8–12 weeks of age) were randomly divided into two groups to receive LPS or saline treatment (n = 6 for each group), as described above. Six hours after the intratracheal instillation of LPS or saline, a pair of mice were anesthetized using 1 % isoflurane via a face mask and loaded directly on the top of the iQID system for dynamic [99mTc]Tc-HA10 imaging. The animals were positioned such that their whole bodies were in the central field of view of the iQID camera. [99mTc]Tc-HA10 was simultaneously injected in each via tail vein catheters. Immediately after injection, the mice were imaged for one minute to show cardiac blood pool activity. Subsequent images were acquired every 5 min up to 35 min post-injection. The mice recovered from anesthesia and underwent repeated static 15-min acquisitions at 60, 120, and 180 min.

2.12. iQID imaging analysis

A computerized region-of-interest (ROI) analysis was performed using a MATLAB program developed at the University of Arizona for quantitative analysis of [99mTc]Tc-HA10 distribution. ROIs were set over the lungs, cardiac blood pool, and remote soft tissue background. The radioactive counts measured by ROI analysis were corrected by the ROI size (number of pixels), radioactive decay, and acquisition time to generate time-activity curves (TACs). Using TableCurve 2D software (Systat Software, Inc., San Jose, CA), we measured the kinetics of [99mTc]Tc-HA10 by fitting TACs with the estimation methods described previously [46,47]. The curve fitting used a set of kinetic functions with or without an equilibrium [48]. We applied exponential equations with no equilibrium when a TAC did not reach a constant level by the end of

the imaging session. We determined the kinetic parameters of [^{99m}Tc]Tc-HA10 from the equation set, including washout half-time (time to 50 % of peak activity, $T_{1/2}$) for the fast and slow components and equilibrium (residual activity retention) of each animal.

2.13. [^{99m}Tc]Tc-HA10 biodistribution measurement and lung autoradiography

All mice were sacrificed at the end of the imaging session, and samples of blood, heart, lungs, liver, spleen, stomach, intestine, kidneys, submandibular glands, skin, and skeletal muscle were harvested. The tissue samples were weighed, and the radioactivity was measured to obtain the biodistribution data (%ID/g). After biodistribution measurement, the distribution of [^{99m}Tc]Tc-HA10 radioactivity in the lung was examined using autoradiography. The left and right lungs were covered with one layer of plastic wrap and exposed to FujiFilm phosphor imaging plates for 1–5 min. A FujiFilm BAS5000 Bio-Imaging Analysis System (Stamford, CT) was used to scan the plates for digital autoradiograph collection.

2.14. Ethics

Animal experiments were performed following the Principles of Laboratory Animal Care from the National Institutes of Health (NIH Publication 85-23, revised 1985). Animal protocol for the experiments was approved by the Institutional Animal Care and Use Committee (IACUC) at the University of Arizona.

2.15. Data analysis

Data collected in the experiments and image analyses were entered into Microsoft Excel 2016 spreadsheets. All quantitative results were expressed as mean ± S.E.M. Statistical analysis was performed using SigmaPlot 12® (Systat Software, Inc., San Jose, CA). Comparisons between two variables were performed with a one-way analysis of variance. A probability (*P*) value <0.05 was considered significant.

3. Results

3.1. Radiolabeling of HA10

^{125}I-iodination of HA10 via Tyr generated a 70–75 % radiochemical yield of [^{125}I]I-Tyr-HA10 as determined by ITLC analysis. After gel filtration, RCP was >96 %. The specific activity of [^{125}I]I-Tyr-HA10 was 3.3–3.5 GBq/mM. When the reactive aromatic Tyr derivative, TA, was attached to the HA10 molecule and generated an alternative [^{125}I]I-TA-HA10, the radiochemical yield of [^{125}I]I-TA-HA10 was similar to [^{125}I]I-Tyr-HA10 in the range of 70–75 %. The specific activity of [^{125}I]I-TA-HA10 was 3.4–3.6 GBq/mM.

The production of [^{99m}Tc]Tc-HA10 is advantageous compared to the 70–75 % labeling yield of [^{125}I]I-TA-HA10, which requires precursor synthesis. Under mild labeling conditions and neutral pH during the reaction, direct ^{99m}Tc-labeling of HA10 always generated >95 % yield. As determined by SEC-HPLC analysis, a minimal amount of free ^{99m}Tc was detected in the [^{99m}Tc]Tc-HA10 products. Radioactivity recovery of labeled HA10 off the HPLC column was always >95 %. After gel-filtration purification, the labeled products of [^{99m}Tc]Tc-HA10 were consistently obtained at ~100 %. Representative HPLC chromatograms of purified [^{99m}Tc]Tc-HA10 and non-labeled HA10 are presented in Fig. 3. The specific activity of [^{99m}Tc]Tc-HA10 was 3.0–3.6 GBq/mM. Compared with direct labeling, using GH as an exchange ligand did not increase the initial yield of radiolabeling HA10; it also did not stabilize the product but decreased the stability of [^{99m}Tc]Tc-HA10 over 5 h.
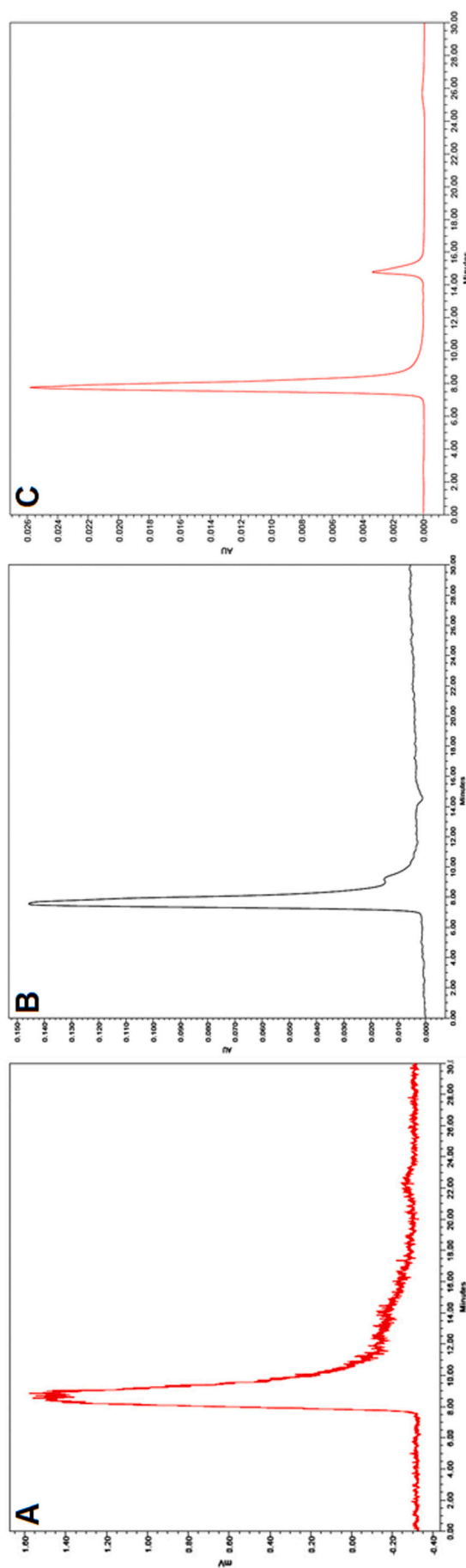

Fig. 3. HPLC chromatograms. A: Radiochromatogram of purified [^{99m}Tc]Tc-HA10 product. B and C: UV (280 nm) chromatograms of ^{99m}Tc-labeled HA10 (B) and non-labeled HA10 (C).

3.2. Stability of radiolabeled HA10

Based on RCP measurements by iTLC, [^{125}I]I-TA-HA10 exhibited less degradation than [^{125}I]I-Tyr-HA10 after 5-h incubation at 37 °C in rat serum. RCP at 30 min post-purification was 98.66 ± 0.47 % for [^{125}I]I-TA-HA10 and 98.22 ± 0.42 % for [^{125}I]I-Tyr-HA10 ($P > 0.05$, n = 5). Five hours after incubation with serum, the measurement of RCP was 96.9 ± 0.5 % for [^{125}I]I-TA-HA10 and (94.8 ± 0.3 %, $P < 0.05$) for [^{125}I]I-Tyr-HA10.

[^{99m}Tc]Tc-HA10 product from the direct ^{99m}Tc-labeling protocol had more reasonable thermodynamic stability than the GH ligand exchange protocol. After 5-h incubation in rat serum at 37 °C, the RCP of [^{99m}Tc]Tc-HA10 decreased from 98.2 ± 0.51 % at 30 min post-purification to 94.6 ± 1.5 % for the directly labeled product ($P > 0.05$, n = 5). In contrast, the RCP of the radiolabeled product via the ligand exchange decreased to 91.9 ± 2.4 % from 98.2 ± 0.74 % ($P < 0.05$, n = 5).

3.3. iQID imaging of [^{125}I]I-TA-HA10 and [^{99m}Tc]Tc-HA10 in healthy mice

Representative iQID images of [^{125}I]I-TA-HA10 and [^{99m}Tc]Tc-HA10 biodistribution in healthy mice are shown in Fig. 4A and B. The distribution of each radiolabeled HA10 complex was prominently present in the liver and spleen. A moderate amount of radioactivity was observed in the kidneys and bladder. Radioactive uptake was visible in the thyroid on [^{125}I]I-TA-HA10 images, possibly due to ^{125}I deiodination from iodinated-HA10 molecules. The overall image quality of [^{99m}Tc]Tc-HA10 was superior to that of [^{125}I]I-TA-HA10, as evidenced by the higher radioactive background of soft tissue seen on [^{125}I]I-TA-HA10 images. Radioactive uptake of [^{99m}Tc]Tc-HA10 in the thyroid, salivary gland, and stomach was not noticeable. A summary of ex vivo biodistribution data of [^{125}I]I-TA-HA10 and [^{99m}Tc]Tc-HA10 is presented in Fig. 4C. Except for the significantly higher uptake of [^{99m}Tc]Tc-HA10 in the liver, there were no significant differences in radioactive uptake in major organs between [^{99m}Tc]Tc-HA10 and [^{125}I]I-TA-HA10.

3.4. [^{125}I]I-TA-HA10 and [^{99m}Tc]Tc-HA10 uptake in mouse models of skin injury and wound healing

Autoradiographs of mouse ears were collected after 4 h of radiotracer injection. As shown in Fig. 5A and B, the radioactive levels of [^{125}I]I-TA-HA10 and [^{99m}Tc]Tc-HA10 in the control ears were minimal. In contrast, the inflamed ears showed markedly increased radioactive uptake corresponding to promoted HA deposition shown on HA IHC staining of ear sections.

After two TPA treatments, inflamed right ears appeared with noticeable dermal and epidermal thickening compared to control left

ears. Relative to the normal histological appearance of control left ears (Fig. 5C), TPA-injured skin was characterized by epidermal hyperplasia and inflammatory changes, including vascular dilation, edema, and infiltration of polymorphonuclear leukocytes (Fig. 5D). HA IHC staining showed that HA was predominantly distributed in the epidermis, subcutaneous glands, and orifices of hair follicles in healthy skin (Fig. 5E). Most of the epidermis was moderately positive in HA staining and exhibited a diffuse pattern. Subcutis or hypodermis was either negative or weakly positive. In contrast, TPA-treated ears showed significantly increased HA deposition throughout the epidermis and dermis (Fig. 5F).

The results of ear thickness measurement and [^{99m}Tc]Tc-HA10 uptake in the mice with chronic skin inflammation and wound healing are shown in Fig. 6. Five mice that received excessive HA35 administration survived well and exhibited no observed adverse effects compared to the mice of the control group with saline. TPA-injured ears with five doses of HA35 showed a 25.8 % reduction of dermal swelling compared to the ears with saline administration. [^{99m}Tc]Tc-HA10 uptake (%ID/g) in the injured right ears with and without HA35 protections showed an averaged 27.7 % difference (0.29 ± 0.02 vs. 0.40 ± 0.09, $P < 0.01$). No difference was observed in the control ears between the two groups (0.15 ± 0.03 vs. 0.13 ± 0.03, $P > 0.05$).

3.5. Inflammatory response and native HA expression in the lungs with ARDS

Representative microphotographs of sectioned lung samples with H&E staining and HA staining by affinity histochemistry assay are shown in Fig. 7. H&E stained sections from the LPS-treated lungs showed an alveolar inflammatory appearance with significantly increased inflammatory cell infiltration, alveolar edema, and thickening compared to the lung sections of control mice. Microscopic images of the lungs from the control group revealed the typical structure and no histopathological changes. HA staining showed significantly increased intracellular HA expression, substantial deposition in the lung alveoli, and thickening of the perialveolar interstitium and perivascular tissues. The control mice showed moderate HA staining at intact alveolar walls, the epithelial cell-extracellular matrix interface, and perivascular tissue. Using computerized image analysis for quantitative measurement of positive HA staining on the lung sections, the lungs treated with LPS demonstrated more extensive and higher intensity HA deposition in the interstitial and intra-alveolar sites, as presented in Table 1.

The results of lung HA content, as measured by ELISA assay from LPS-treated mice and saline controls, are also presented in Table 1. There was a statistically significant difference in the HA concentration (ng/mL) of lung homogenate between the LPS-treated mice and controls (9723.6 ± 658.0 vs. 6376.1 ± 779.5, $P = 0.039$, n = 5 each group). The higher HA content in the lungs with ARDS corresponded to findings on
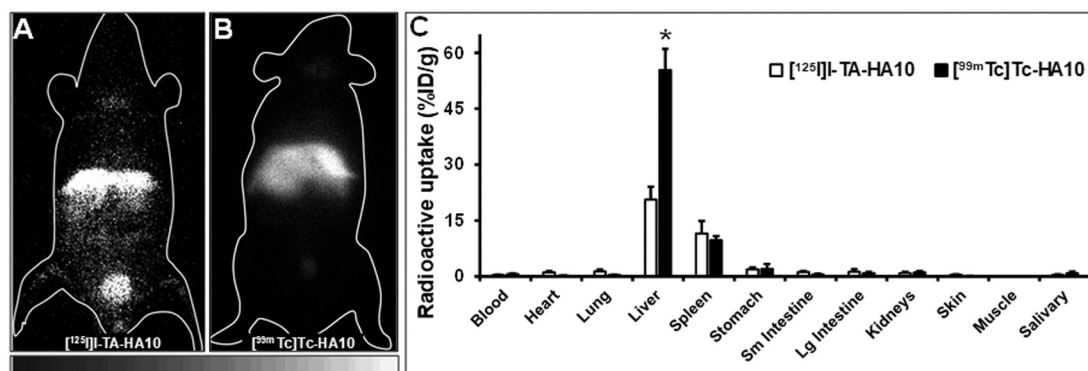
Fig. 4. Representative in vivo iQID images of [^{125}I]I-TA-HA10 (A) and [^{99m}Tc]Tc-HA10 (B) in healthy mice. Under isoflurane (1.0–1.5 %) anesthesia, the mice were imaged for 15 min at 3 h post-injection of [^{125}I]I-TA-HA10 (200 μCi) and [^{99m}Tc]Tc-HA10 (1.0 mCi). C: Biodistribution measurements of [^{125}I]I-TA-HA10 and [^{99m}Tc]Tc-HA10 in healthy mice (n = 5 each group) after 3 h of radiotracer injection. * $P < 0.001$ compared to [^{125}I]I-TA-HA10.
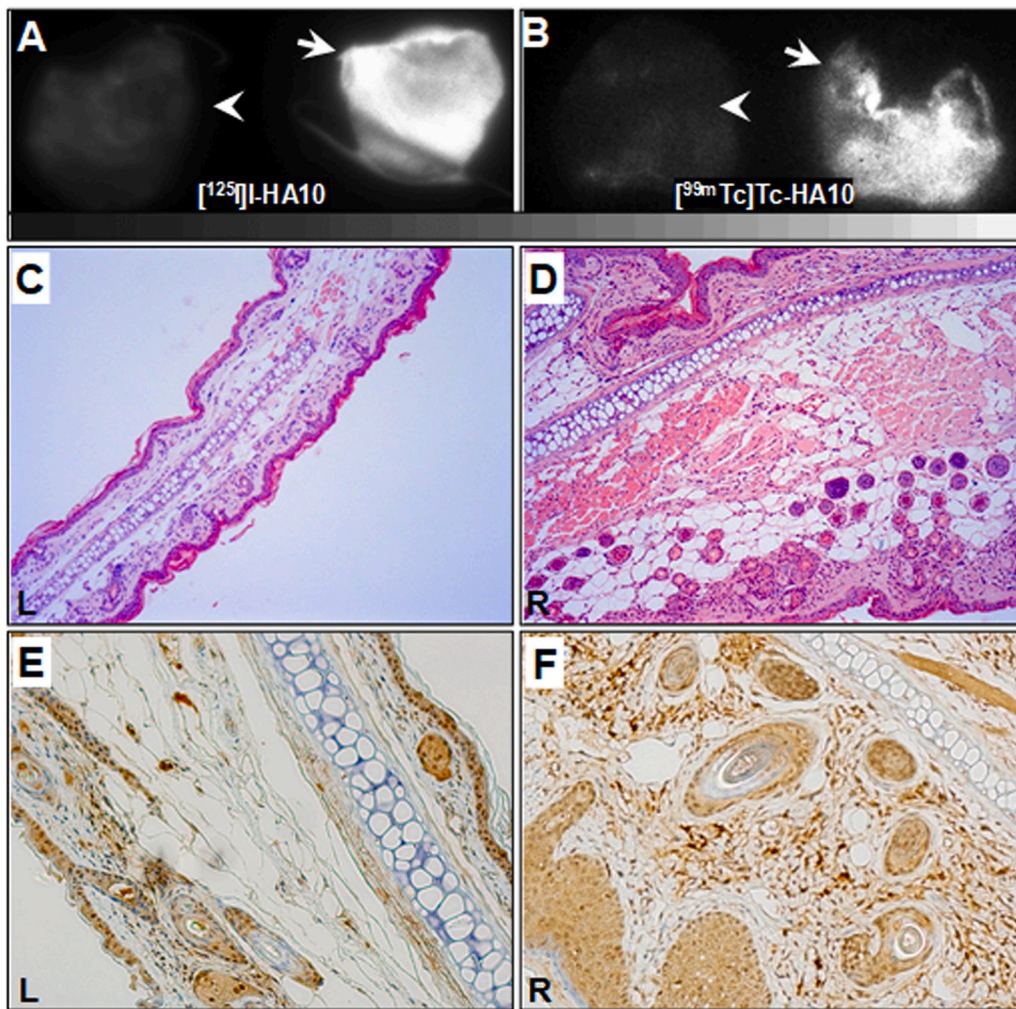
Fig. 5. A and B: Representative autoradiographs of [^{125}I]I-TA-HA10 (A) and [^{99m}Tc]Tc-HA10 (B) in mouse ears treated with TPA (marked by arrows) and acetone control (marked by arrowheads). Significantly increased radioactive uptake was present in the TPA-treated ears. C and D: Photomicrographs of H&E-stained tissue sections (5 µM) taken from mouse ears treated with acetone (C) and experimental TPA (D). The micrograph of the TPA-treated ear shows marked thickening and infiltration within the deeper tissue compared to the normal histological appearance of the control ear with acetone. E and F: Photomicrographs of HA IHC staining in control ear (E) and TPA-injured ear (F) demonstrating extensively increased HA deposition in the inflamed skin relative to the moderate HA expression in the non-inflamed skin.

histological examination with HA staining.

3.6. iQID dynamic images and kinetic profile of [^{99m}Tc]Tc-HA10 in mice with ARDS

Representative iQID dynamic images of [^{99m}Tc]Tc-HA10 from a mouse that received LPS and a control mouse are shown in Fig. 8. After intravenous injection, [^{99m}Tc]Tc-HA10 was quickly delivered into the cardiac blood pool and distributed to the body. While radioactivity of the cardiac and lung blood pool became visible at 1-min post-injection, [^{99m}Tc]Tc-HA10 was already distributed in the liver, spleen, and kidneys and increased afterward. From 2 min to 194 min, radioactivity in the control mice was predominantly present in the liver, spleen, and kidneys, with transient bladder activity. Radioactive clearance from the lungs of control mice was very fast, resulting in significantly lower pulmonary retention by 30 min post-injection than that in LPS-treated mice. From 1 to 194 min after tracer injection, radioactivity in the liver was consistently higher than in the lungs. Salivary glands were barely visible in the control animals in 60–194 min post-injection. In contrast, the LPS-treated mice showed increased [^{99m}Tc]Tc-HA10 uptake in the lungs and a slow washout of radioactivity. Typically, the lung radioactivity was higher than the liver during the first hour and then became equivalent to or lower than the liver activity but remained at the significantly elevated level up to 194 min post-injection compared to the residual activity of control lungs. Unlike in the images of control mice, the radioactive uptake in both thyroid and submandibular salivary glands was noticeable in the dynamic images of LPS-treated mice. The thyroid became visible about 10 min after injection. The submandibular salivary glands were visualized after 60 min of [^{99m}Tc]Tc-HA10.

TACs of the cardiac blood pool and lungs, derived from dynamic iQID images, are presented in Fig. 9. Average counts per pixel were determined by applying ROIs established on the 1-min image to the rest of the dynamic images to generate the TACs. Radioactivity at each time point was corrected for background activity, decay, and acquisition time and then normalized to the peak activity at 1-min post-injection. The maximum level of [^{99m}Tc]Tc-HA10 at 1-min in the cardiac blood pool and the lungs was considered to be the peak activity, as shown in the curves in Fig. 9. It was found that biexponential equations with no equilibrium best described the kinetic profiles of [^{99m}Tc]Tc-HA10 in the lungs. There was no significant difference in [^{99m}Tc]Tc-HA10 uptake between the left and right lung activity in control or LPS-treated mice. The lung images of control mice exhibited a continuous fast radioactive washout pattern compatible with the quick clearance feature from the cardiac blood pool. Lung radioactivity in the LPS-treated mice presented a slow decrease pattern, starting at 30 min and reaching a relatively steady state of about 60 min. As a result, the significantly higher residual activity of [^{99m}Tc]Tc-HA10, or retention (%), was observed in the lungs of LPS-treated mice at each time point from 60 min to 180 min. At the end of data acquisition, lung activity in the LPS-treated mice was about 2.4-fold higher than in the control mice. The kinetic results of [^{99m}Tc]Tc-HA10 in the cardiac blood pool and lungs, including Peak Activity, $T_{1/2}$ (min), Retention (%), and Fractional Washout (%), are summarized in Table 2.
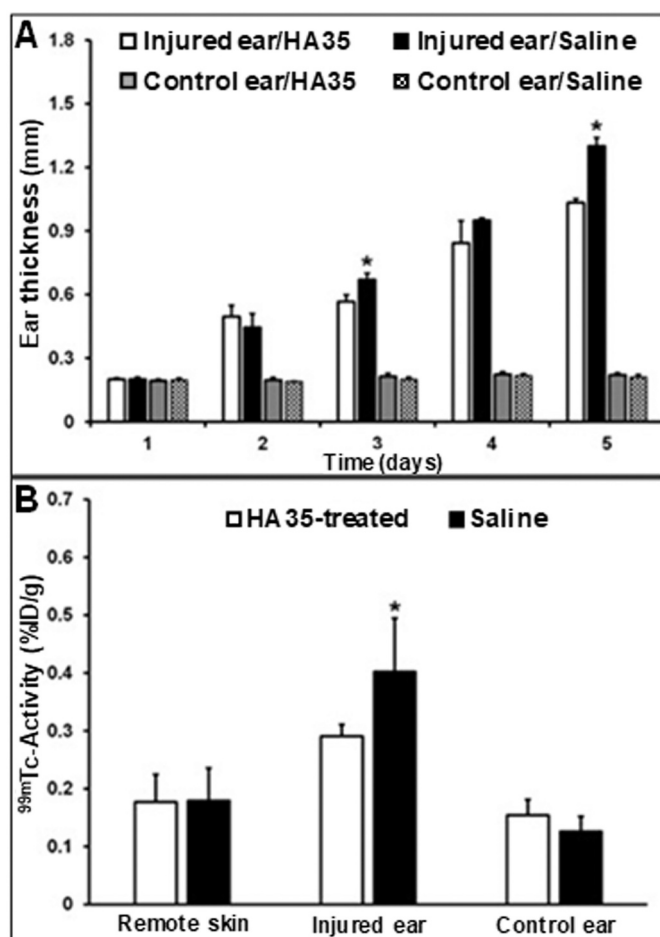
Fig. 6. A: Inhibitory effects of intraperitoneal administration of HA35 (n = 5) on TPA-induced ear edema compared to carrier vehicle saline (n = 5) based on ear thickness changes. B: Ex vivo measurement results of [^{99m}Tc]Tc-HA10 uptake in the remote skin of the thigh, TPA-injured right ears, and acetone-treated left ears. The TPA-injured ears in mice pre-treated with HA35 exhibited less radioactive uptake than in mice with saline (* $P < 0.05$).

3.7. Biodistribution and autoradiography of [^{99m}Tc]Tc-HA10 in LPS-treated and control mice

The biodistribution results of [^{99m}Tc]Tc-HA10 in the blood and major organs of two groups treated with intratracheal instillation of LPS and saline are summarized in Table 3. The liver and spleen were the organs with the highest [^{99m}Tc]Tc-HA10 uptake. The stomach showed a notably higher level of radioactivity than other organs, including the heart, kidney, and intestine. The blood activity of [^{99m}Tc]Tc-HA10 in the group with LPS administration was significantly higher than in the group with saline instillation. LPS-treated lungs demonstrated 8.1-fold higher [^{99m}Tc]Tc-HA10 uptake than the controls ($P < 0.001$). Submandibular salivary glands in the mice with intratracheal instillation of LPS had higher [^{99m}Tc]Tc-HA10 uptake compared to the control animals ($P < 0.05$).

4. Discussion

In healthy lungs, HA molecules are primarily located within the airway submucosa and pulmonary vasculature walls but exist lesser in the alveoli. HA expression is regulated by regional HA synthase activity and degradation by hyaluronidase. Aberrant HA production from mast cells, epithelial cells, endothelial cells, and fibroblasts following severe lung virus infection leads to the formation of HA-enriched extracellular

matrix (ECM), excess accumulation of HA in the airway lumen, and intracellular distribution [14,15,49,50].

HA is a dynamic molecule that can differentially promote or inhibit pathology based on its molecular weight and accessibility to various hyaladherins, also known as hyaluronan binding proteins (HABPs), such as CD44, TLR4, and RHAMM [2,13,20]. HA with high molecular weight is located in the peribronchial and perialveolar regions of the lungs, providing structural integrity and displaying anti-inflammatory properties. In viral infections such as COVID-19, HA can form cable-like structures that disrupt tissue architecture and cause biophysical rigidity [14,16,17]. Excess accumulation of water induced by HA outpouring in the ECM and airway lumen impairs pulmonary oxygenation and can lead to death in high-risk ARDS. Small HA fragments that occur due to upregulated hyaluronidase activity and reactive oxygen species (ROS)-mediated mechanisms stimulate the expression of inflammatory genes by various immune cells at the injury site [51]. HABPs having a specific affinity towards the HA fragments regulate inflammation, tissue injury, and repair through enhancing inflammatory cell recruitment, cytokine release, and stem cell migration. In the early phases of ARDS, HA-driven inflammatory response leads to diffuse alveolar damage by alveolar flooding of proteinaceous fluid with hyaline membrane deposition on the basement membranes. Fibroproliferative processes predominate in the late phase of ARDS. Similar progression in the severity and potential irreversibility is seen in the COVID-19-related ARDS (CARDS) [52]. Visualizing HA levels in the lungs and their response to therapy would be expected to provide valuable insights into the early and timely management of ARDS, especially in COVID-19-related lung damage.

This study investigated the feasibility of radiolabeled HA10 with ^{125}I and ^{99m}Tc to assess tissue inflammatory responses. Because HA does not have a suitable functional group for labeling with radioiodine, an active phenol group from Tyr or TA must be introduced by reductive amination. We found that [^{125}I]I-TA-HA10 exhibits higher stability and improved biodistribution than [^{125}I]I-Tyr-HA10. Our in vivo imaging results indicate that [^{125}I]I-TA-HA10 can be used to localize inflammatory sites and has biodistribution comparable to [^{99m}Tc]Tc-HA10. The ^{125}I-iodination protocol for HA10 labeling may be used with ^{123}I (half-life 13.3 h and gamma energy 159 keV) to produce ^{123}I-iodinated TA-HA10 agents for clinical imaging of patients with HA-upregulated diseases, such as ARDS.

^{99m}Tc was chosen as the preferred radiolabel for HA in this study for its optimal nuclear properties (half-life 6 h, gamma energy 140 keV) and its ability to be directly anchored to the HA polymer, resulting in stable radiolabeled species. Each HA molecule contains many functional groups that can bind reduced pentavalent ^{99m}Tc. ^{99m}Tc labeling of HA molecules leads to only minor changes of the polysaccharides in charge, conformation, and hydrophilicity without significant changes in their biodistribution and physiological interactions [53]. We investigated two protocols with and without GH as an exchange agent for ^{99m}Tc-labeling HA10 to obtain a high yield and stable product. It was found that the addition of GH did not stabilize the outcome of [^{99m}Tc]Tc-HA10 but instead decreased the stability of labeled HA10, possibly because the chemical structure of GH is similar to that of HA, and it, therefore, acts as a competitor instead of an exchange ligand [25]. Our in vitro stability and in vivo imaging data demonstrated that [^{99m}Tc]Tc-HA10 prepared by direct ^{99m}Tc-labeling of HA10 was relatively stable enough for hours to reach the target tissues. After 60 min post-injection, salivary glands on iQID dynamic images became visible in the mice with intratracheal instillation of LPS but were barely detectable in the control mice. However, no further radioactivity increase was observed in the glands of LPS-treated mice from 60 to 194 min post-injection, indicating that the significant activity might not be from pertechnetate, which is the decomposition product of [^{99m}Tc]Tc-HA10. The measurement of post-mortem biodistribution showed the submandibular gland radioactivity in the LPS-treated mice was significantly higher than in the control mice, indicating that the increased radioactivity might mainly result from [^{99m}Tc]Tc-HA10 deposit related to the inflammatory response. Based on
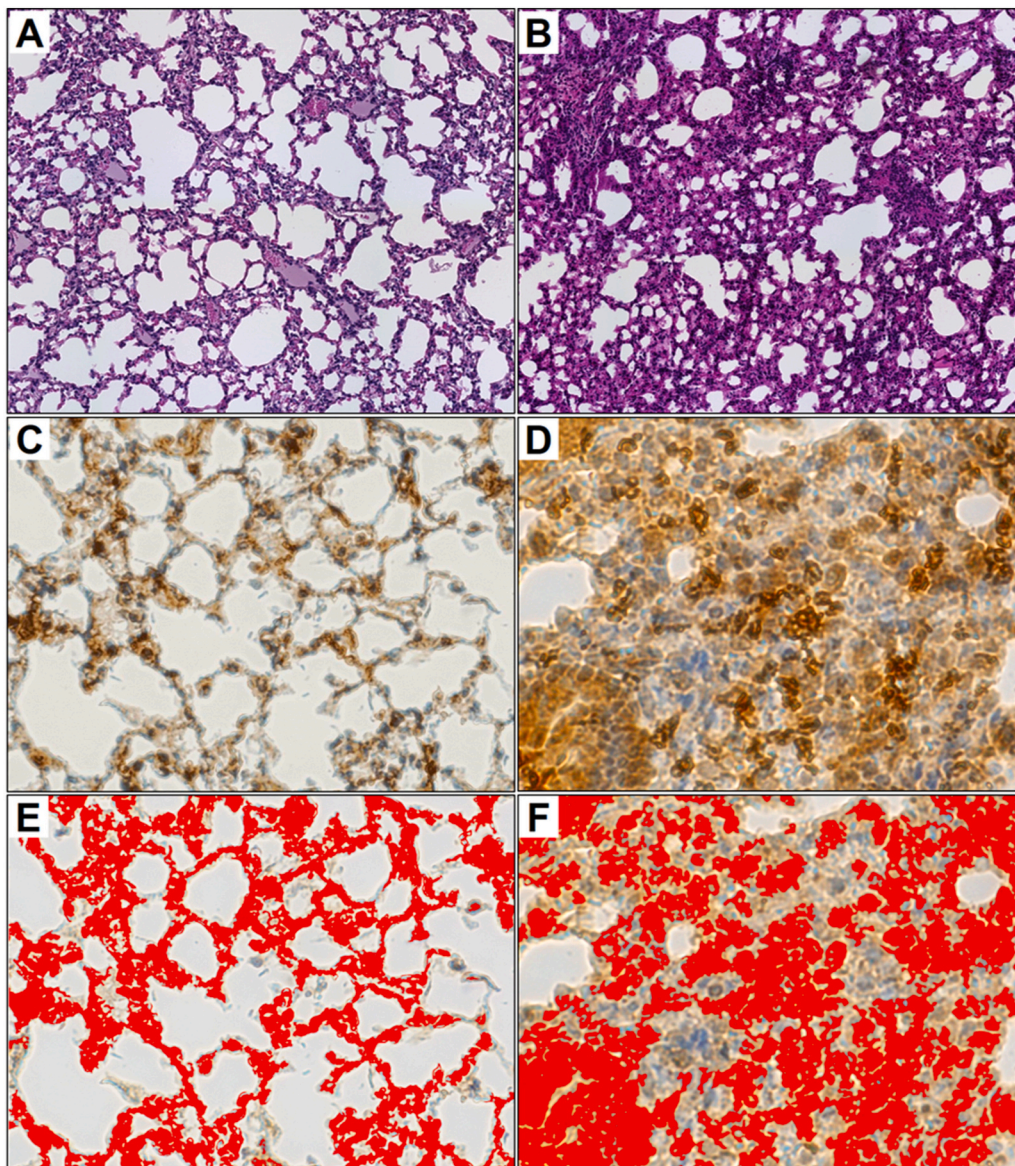
Fig. 7. Representative photomicrographs of H&E- (A and B) and HA IHC-stained sections (C and D) of lung tissues from a control mouse with saline (A and C) and a mouse model of LPS-induced ARDS (B and D). Relative to the normal lung architecture and moderate HA expression in control, the lung section from the LPS-treated mouse showed alveolar wall thickening, inflammatory cell infiltration, and markedly increased HA deposition, as illustrated by overlays in red by Fill Measurement of SigmaScan (E and F). (For interpretation of the references to color in this figure legend, the reader is referred to the web version of this article.)

Table 1
Results of HA expression in the lungs by IHC and ELISA.

|	HA+ Area (%)	HA Intensity (OD)	HA Content (ng/mL)
	IHC		ELISA
LPS (n = 5)	64.0 ± 3.1*	72.7 ± 1.0*	9723.6 ± 658.0*
Saline (n = 5)	33.0 ± 2.8	57.1 ± 0.9	6376.1 ± 779.5

OD: optical density.
* $P < 0.01$ compared to saline control.

dynamic imaging up to 194 min, the stomach radioactive uptake did not interfere with visualization of [99mTc]Tc-HA10 distribution in other organs even though the biodistribution measurements showed that the stomach activity after 194 min post-injection was statistically higher than the kidneys and intestine probably due to slowly decreased RCP and released free 99mTc.

Our hypothesis that radiolabeled HA10 agents could delineate HA involvement in inflammatory reactions was first verified in the mouse model of TPA-induced skin inflammation [35,36,54,55]. TPA is a well-established pro-inflammatory agent that stimulates inflammatory cytokine release, tissue edema, epidermal thickening, and cornified envelope formation when topically applied. TPA application triggers the recruitment of leukocytes that have roles in modulating epidermal responses and regulating fibroblast differentiation into myofibroblasts. Consistent with previous studies that induction of HA in the murine epidermis with TPA-induced injury persisted for at least one week [54,56], our study up to 5 days showed that significantly increased skin uptake of radiolabeled HA10 was correlated with inflammatory intensity. Furthermore, we found that administering HA35 promoted wound healing in mice with TPA-induced ear injury. Due to the concern of low stability and short biological half-life of extraneous HA, our mouse model with skin wound healing was given an excessive dose of the size-specific HA35 via intraperitoneal injection. The exceeding dose (20 mg/day) of HA35 did not cause unacceptable adverse effects in the mice. The beneficial effect of HA35 on wound healing might be mediated through induction of epithelial proliferation, elicitation of epithelial β-defensins, and increased expression of tight junction protein zonula occludens (ZO)-1 [57–59]. Previous studies have shown that exogenous, specific-sized HA of an average molecular weight of 35 kDa diminished inflammatory responses in murine models of inflammation, including bacterial-driven colitis and alcohol-mediated injury [59–62]. HA fragments of 5–20 kDa are believed to be pro-inflammatory and have no healing effects. Thus,
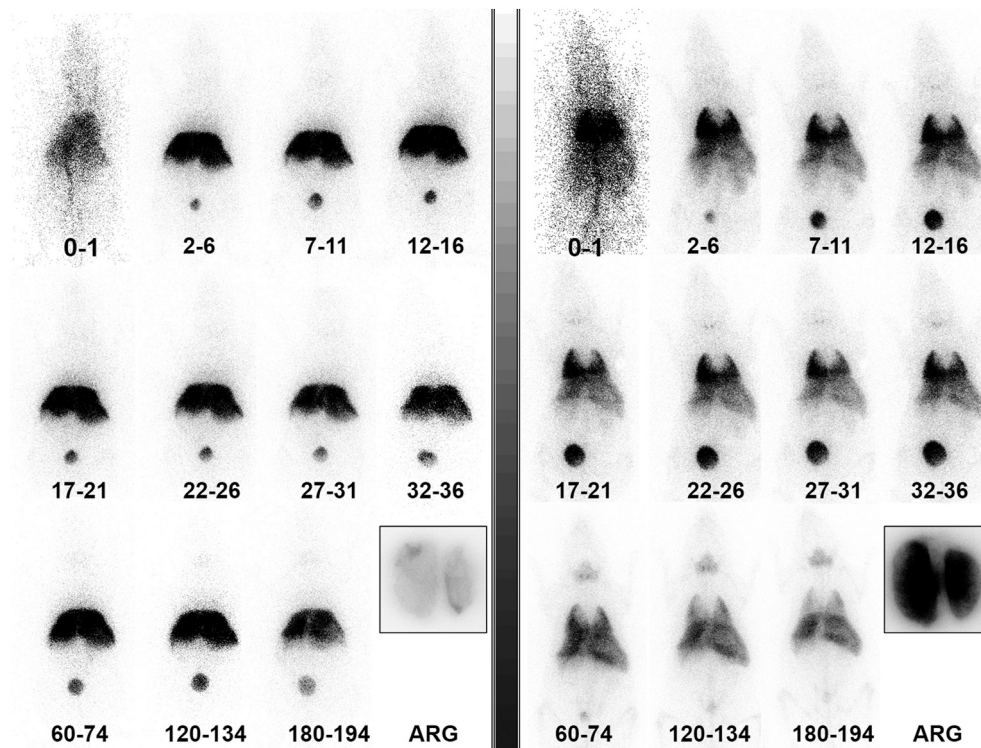
Fig. 8. Representative dynamic iQID images of [^{99m}Tc]Tc-HA10 from a control mouse (*Left panel*) and a mouse with LPS-induced ARDS (*Right panel*) under isoflurane anesthesia (1.0–1.5 %). The dynamic images were acquired immediately after intravenous radiotracer injection (1.0 mCi, 0.2 mL). Relative to the control mouse, remarkably higher [^{99m}Tc]Tc-HA10 deposition was observed in the lung with ARDS. The numbers below individual images are times post tracer injection and duration of image acquisition. ARG: autoradiography.
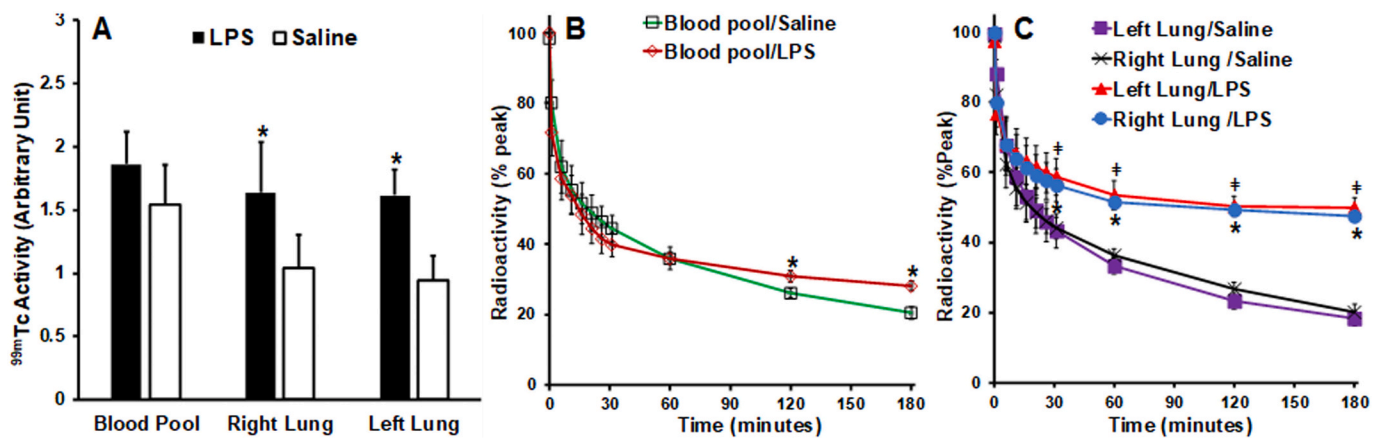
Fig. 9. A: Summarized peak radioactivity of [^{99m}Tc]Tc-HA10 determined by iQID imaging. B and C: [^{99m}Tc]Tc-HA10 time-activity curves (TACs) of the cardiac blood pool (B) and lungs (C) generated by ROI analysis of iQID images acquired from mice treated by LPS (n = 6) and saline (n = 6). The radioactivity at each time point of TACs was normalized by individual peak radioactivity as 100 %. * *P* < 0.05 compared to control.

Table 2
Kinetic results of [^{99m}Tc]Tc-HA10 of the cardiac blood pool and lungs.

	Peak (p.d.u.)		T$_{1/2}$ (min)		Retention (%)		Washout (%)	
	Ctrl	LPS	Ctrl	LPS	Ctrl	LPS	Ctrl	LPS
Blood	1.5 ± 0.3	1.9 ± 0.3	16.98 ± 5.7	13.84 ± 4.4	20.49 ± 1.8	28.2 ± 1.4	79.5 ± 1.8	71.8 ± 1.4
Lung/L	1.0 ± 0.2	1.6 ± 0.2	21.3 ± 5.7	103.2 ± 33.9*	18.5 ± 2.1	49.9 ± 2.9*	81.5 ± 2.1	50.1 ± 2.9*
Lung/R	1.0 ± 0.3	1.6 ± 0.4	19.0 ± 4.9	105.8 ± 26.6*	20.2 ± 2.4	47.6 ± 1.8*	79.8 ± 2.4	52.4 ± 1.8*

p.d.u. procedure defined unit or arbitrary unit.
* *P* < 0.05 compared to Control (Ctrl).

Table 3
[^{99m}Tc]Tc-HA10 biodistribution (%ID/g).

Tissue	LPS-treated	Saline control
Blood	1.72 ± 0.52*	0.75 ± 0.37
Heart	0.42 ± 0.11	0.49 ± 0.18
Lungs	10.97 ± 3.89*	1.35 ± 0.30
Liver	42.61 ± 6.87	59.09 ± 7.28
Spleen	23.59 ± 5.38	23.39 ± 8.53
Stomach	4.34 ± 1.43	3.39 ± 1.69
Small intestine	0.84 ± 0.19	0.71 ± 0.22
Large intestine	0.53 ± 0.13	0.76 ± 0.32
Kidneys	1.51 ± 0.39	1.18 ± 0.54
Skin	0.34 ± 0.07	0.19 ± 0.06
Muscle	0.10 ± 0.02	0.06 ± 0.02
Salivary glands	5.78 ± 1.88*	1.65 ± 0.89

* *P* < 0.05 compared to saline control.

the uptake of radiolabeled HA10 at the site of skin wound healing provides a measure to monitor injury attenuation and therapeutic responses. Our findings in this study indicate that exogenous HA10 may play a multifaceted role as a theranostic biomarker involving specific mediation of cellular and matrix events via cell receptors or binding proteins and nonspecific accumulation caused by the osmotic activity of HA.

In physiological conditions, the lungs eliminate HA fragments derived from larger molecular weight HA chains using active transport processes, including mucociliary transport, macrophage clearance, and passive diffusion to the bloodstream or lymph [26]. Macrophages with bound or phagocytosed HA can sequester HA and clear the pulmonary bed through subsequent migration into the draining lymphatics. This study shows that most HA molecules can be removed quickly from healthy lung tissues, where >80 % washout of initial [^{99m}Tc]Tc-HA10 uptake occurred by the end of the 3-hour imaging session. In ARDS, such as LPS-induced pulmonary injury in this study, the lung parenchyma is damaged by the generation and release of proteases, ROS, and RNS produced by activated lung macrophages and neutrophils in the interstitial and alveolar compartments. LPS is further associated with pulmonary endothelial barrier disruption. Upon tissue damage, proinflammatory cytokines, such as TNFα and IL-1β, induce HA overproduction and degradation from large molecules into smaller fragments via ROS and reactive nitrogen species (RNS), which can act as mediators that activate the innate immune response associated with the pathophysiology of ARDS [63–65]. Following the supranormal HA outpouring over a short time in lungs with ARDS, HA fragments accumulated in the edematous alveolar septa leak into the alveoli due to disruption of alveolar-capillary membrane integrity [12,26,66–68]. Mucociliary dysfunction, elimination of damaged macrophages, and interrupted pulmonary lymphatic drainage result in extensive deposition of HA with high water-binding capacity in the lungs, resulting in pulmonary edema, asphyxia, and eventually acute cardiopulmonary failure. Significant increases in lung weights are found at autopsy in confirmed COVID-19 victims, as are histologic findings of "hyaline membranes" that have also been described in non-COVID ARDS, influenza A (H1N1), SARS, and MERS autopsies [24,69]. The imaging data reported in this work represent the first application of radiolabeled HA10 with the iQID camera to delineate HA metabolism and dynamics in the lungs of mice with ARDS.

Biologically, HA fragments might bind to various cell receptors, including CD44, RHAMM, hyaluronan receptor for endocytosis (HARE), TLR2, and TLR4. These receptors are actively involved in the signaling pathways of ARDS-associated CRS [7,18,19], which is also a hallmark change with increased vascular permeability. Based on the evidence of increased endogenous lung HA expression, inflammatory cell recruitment, and pulmonary edema in the mouse model with LPS instillation, it is likely that increased pulmonary uptake of [^{99m}Tc]Tc-HA10 is associated with upregulated receptor binding, enhanced cellular internalization, promoted concentration-dependent HA deposition, accelerated permeability in the pulmonary stroma and alveoli, and disturbed HA elimination [70]. In addition, systemically-administered exogenous HA fragments might deposit like endogenous HA molecules in the pulmonary interstitium and form larger complexes that resist removal due to the self-aggregating properties of polysaccharides [71,72]. Thus, [^{99m}Tc]Tc-HA10 might partly act like a larger HA fragment and retain a higher level of deposition in the lung parenchyma with dysfunctional elimination.

We found in the present study that [^{99m}Tc]Tc-HA10 imaging may detect inflammatory responses of submandibular salivary glands in the profile of LPS-induced remote organ and tissue inflammation [73–75]. Rodent salivary glands can exert a neuroimmunomodulatory influence on distant inflammatory events. This pathophysiological phenomenon in the submandibular glands may reflect pulmonary inflammatory responses via proinflammatory cytokines, such as IL-1β, IL-6, and TNFα, induced by LPS via TLR2 and TLR4. HA fragments can signal through TLR2 and TLR4 to trigger innate immunity in immune cells. Thus, increased [^{99m}Tc]Tc-HA10 uptake in the submandibular salivary glands may indicate upregulated expression of TLR2/TLR4 in the saliva in response to endotoxin.

5. Conclusions

We investigated the utility of radiolabeled HA10 in quantitative imaging of mouse models of inflammatory diseases using a high-resolution iQID camera. Imaging data were compared to histological and immunochemical findings. In the mouse model of ear inflammation, the uptake of radiolabeled HA10 paralleled histologic findings of tissue inflammation; [^{99m}Tc]Tc-HA10 and [^{125}I]I-TA-HA10 had similar biodistribution. [^{99m}Tc]Tc-HA10 imaging with iQID camera showed promising results for assessing focal inflammatory responses and injury attenuation. Dynamic imaging of [^{99m}Tc]Tc-HA10 in the mouse model of ARDS showed markedly increased uptake and persistence of activity in the lungs, consistent with prominent inflammatory changes on postmortem analyses. These findings suggest that [^{99m}Tc]Tc-HA10 has high translational possibilities for clinical imaging in ARDS, such as lung involvement in COVID-19. Measuring the clearance rate of [^{99m}Tc]Tc-HA10 from the lungs by the iQID camera may provide a practical way to investigate the evolution of inflammatory lung changes and the response to therapeutic intervention.

References

[1] Matthay MA, Zemans RL, Zimmerman GA, Arabi YM, Beitler JR, Mercat A, et al. Acute respiratory distress syndrome. Nat Rev Dis Primers 2019;5:18.

[2] Singleton PA, Lennon FE. Acute lung injury regulation by hyaluronan. J Allergy Ther 2011;Suppl 4.

[3] Bellani G, Laffey JG, Pham T, Fan E, Brochard L, Esteban A, et al. Epidemiology, patterns of care, and mortality for patients with acute respiratory distress syndrome in intensive care units in 50 countries. JAMA 2016;315:788–800.

[4] Ramanathan K, Antognini D, Combes A, Paden M, Zakhary B, Ogino M, et al. Planning and provision of ECMO services for severe ARDS during the COVID-19 pandemic and other outbreaks of emerging infectious diseases. Lancet Respir Med 2020;8:518–26.

[5] Hellman U, Karlsson MG, Engstrom-Laurent A, Cajander S, Dorofte L, Ahlm C, et al. Presence of hyaluronan in lung alveoli in severe COVID-19: an opening for new treatment options? J Biol Chem 2020;295:15418–22.

[6] Matsuyama T, Kubli SP, Yoshinaga SK, Pfeffer K, Mak TW. An aberrant STAT pathway is central to COVID-19. Cell Death Differ 2020;27:3209–25.

[7] Moore JB, June CH. Cytokine release syndrome in severe COVID-19. Science 2020;368:473–4.

[8] Nickols J, Obiako B, Ramila KC, Putinta K, Schilling S, Sayner SL. Lipopolysaccharide-induced pulmonary endothelial barrier disruption and lung edema: critical role for bicarbonate stimulation of AC10. Am J Physiol Lung Cell Mol Physiol 2015;309:L1430–7.

[9] Bitker L, Talmor D, Richard JC. Imaging the acute respiratory distress syndrome: past, present and future. Intensive Care Med 2022;48:995–1008.

[10] Bitker L, Dhelft F, Lancelot S, Le Bars D, Costes N, Benzerdjeb N, et al. Non-invasive quantification of acute macrophagic lung inflammation with [(11)C](R)-PK11195 using a three-tissue compartment kinetic model in experimental acute respiratory distress syndrome. Eur J Nucl Med Mol Imaging 2022;49:2122–36.

[11] Esposito AJ, Bhatraju PK, Stapleton RD, Wurfel MM, Mikacenic C. Hyaluronic acid is associated with organ dysfunction in acute respiratory distress syndrome. Crit Care 2017;21:304.

[12] Hallgren R, Samuelsson T, Laurent TC, Modig J. Accumulation of hyaluronan (hyaluronic acid) in the lung in adult respiratory distress syndrome. Am Rev Respir Dis 1989;139:682–7.

[13] Lierova A, Kasparova J, Filipova A, Cizkova J, Pekarova L, Korecka L, et al. Hyaluronic acid: known for almost a century, but still in vogue. Pharmaceutics 2022:14.

[14] Bell TJ, Brand OJ, Morgan DJ, Salek-Ardakani S, Jagger C, Fujimori T, et al. Defective lung function following influenza virus is due to prolonged, reversible hyaluronan synthesis. Matrix Biol 2019;80:14–28.

[15] Reeves SR, Barrow KA, Rich LM, White MP, Shubin NJ, Chan CK, et al. Respiratory syncytial virus infection of human lung fibroblasts induces a hyaluronan-enriched extracellular matrix that binds mast cells and enhances expression of mast cell proteases. Front Immunol 2019;10:3159.

[16] Petrey AC, de la Motte CA. Hyaluronan, a crucial regulator of inflammation. Front Immunol 2014;5:101.

[17] Johnson P, Arif AA, Lee-Sayer SSM, Dong Y. Hyaluronan and its interactions with immune cells in the healthy and inflamed lung. Front Immunol 2018;9:2787.

[18] Ontong P, Prachayasittikul V. Unraveled roles of hyaluronan in severe COVID-19. EXCLI J 2021;20:117–25.

[19] Fajgenbaum DC, June CH. Cytokine storm. N Engl J Med 2020;383:2255–73.

[20] Lennon FE, Singleton PA. Role of hyaluronan and hyaluronan-binding proteins in lung pathobiology. Am J Physiol Lung Cell Mol Physiol 2011;301:L137–47.

[21] Andonegui-Elguera S, Taniguchi-Ponciano K, Gonzalez-Bonilla CR, Torres J, Mayani H, Herrera LA, et al. Molecular alterations prompted by SARS-CoV-2 infection: induction of hyaluronan, glycosaminoglycan and mucopolysaccharide metabolism. Arch Med Res 2020;51:645–53.

[22] Tighe RM, Garantziotis S. Hyaluronan interactions with innate immunity in lung biology. Matrix Biol 2019;78–79:84–99.

[23] Lennon FE, Singleton PA. Hyaluronan regulation of vascular integrity. Am J Cardiovasc Dis 2011;1:200–13.

[24] Barton LM, Duval EJ, Stroberg E, Ghosh S, Mukhopadhyay S. COVID-19 autopsies, Oklahoma, USA. Am J Clin Pathol 2020;153:725–33.

[25] Melendez-Alafort L, Nadali A, Zangoni E, Banzato A, Rondina M, Rosato A, et al. Biokinetic and dosimetric studies of 188Re-hyaluronic acid: a new radiopharmaceutical for treatment of hepatocellular carcinoma. Nucl Med Biol 2009;36:693–701.

[26] Kuehl C, Zhang T, Kaminskas LM, Porter CJ, Davies NM, Forrest L, et al. Hyaluronic acid molecular weight determines lung clearance and biodistribution after instillation. Mol Pharm 2016;13:1904–14.

[27] Laznicek M, Laznickova A, Cozikova D, Velebny V. Preclinical pharmacokinetics of radiolabelled hyaluronan. Pharmacol Rep 2012;64:428–37.

[28] Litwiniuk M, Krejner A, Speyrer MS, Gauto AR, Grzela T. Hyaluronic acid in inflammation and tissue regeneration. Wounds 2016;28:78–88.

[29] Snetkov P, Zakharova K, Morozkina S, Olekhnovich R, Uspenskaya M. Hyaluronic acid: the influence of molecular weight on structural, physical, physico-chemical, and degradable properties of biopolymer. Polymers 2020:12 (Basel).

[30] Miller BW, Gregory SJ, Fuller ES, Barrett HH, Barber HB, Furenlid LR. The iQID camera: an ionizing-radiation quantum imaging detector. Nucl Instrum Methods Phys Res A 2014;767:146–52.

[31] Han L, Miller BW, Barber HB, Nagarkar VV, Furenlid LR. A new columnar CsI(Tl) scintillator for iQID detectors. Proc SPIE Int Soc Opt Eng 2014;9214:92140D.

[32] Veiseh M, Breadner D, Ma J, Akentieva N, Savani RC, Harrison R, et al. Imaging of homeostatic, neoplastic, and injured tissues by HA-based probes. Biomacromolecules 2012;13:12–22.

[33] Gustafson S, Bjorkman T, Westlin JE. Labelling of high molecular weight hyaluronan with 125I-tyrosine: studies in vitro and in vivo in the rat. Glycoconj J 1994;11:608–13.

[34] Cozikova D, Laznickova A, Hermannova M, Svanovsky E, Palek L, Buffa R, et al. Preparation and the kinetic stability of hyaluronan radiolabeled with 111In, 125I and 14C. J Pharm Biomed Anal 2010;52:517–24.

[35] Kim EJ, Park H, Kim J, Park JH. 3,3'-Diindolylmethane suppresses 12-O-tetradecanoylphorbol-13-acetate-induced inflammation and tumor promotion in mouse skin via the downregulation of inflammatory mediators. Mol Carcinog 2010;49:672–83.

[36] Liu Z, Wyffels L, Barber C, Wan L, Xu H, Hui MM, et al. Characterization of 99mTc-labeled cytokine ligands for inflammation imaging via TNF and IL-1 pathways. Nucl Med Biol 2012;39:905–15.

[37] Lilleholt LL, Johansen C, Arthur JS, Funding A, Bibby BM, Kragballe K, et al. Role of p38 mitogen-activated protein kinase isoforms in murine skin inflammation induced by 12-O-tetradecanoylphorbol 13-acetate. Acta Derm Venereol 2011;91:271–8.

[38] Stanley PL, Steiner S, Havens M, Tramposch KM. Mouse skin inflammation induced by multiple topical applications of 12-O-tetradecanoylphorbol-13-acetate. Skin Pharmacol 1991;4:262–71.

[39] Khan I, Dey DK, Lee JH, Kang SC. Bamboo leave extract ameliorated 12-O-tetradecanoylphorbol-13-acetate (TPA) induced ear inflammation by reducing MAP kinase levels and NF-kappaB activation in mice model. Nat Prod Res 2020:1–5.

[40] Chang SN, Khan I, Dey DK, Cho KH, Hwang BS, Bae KB, et al. Decursinol angelate ameliorates 12-O-tetradecanoyl phorbol-13-acetate (TPA) -induced NF-kappaB activation on mice ears by inhibiting exaggerated inflammatory cell infiltration, oxidative stress and pro-inflammatory cytokine production. Food Chem Toxicol 2019;132:110699.

[41] Palumbo S, Shin YJ, Ahmad K, Desai AA, Quijada H, Mohamed M, et al. Dysregulated Nox4 ubiquitination contributes to redox imbalance and age-related severity of acute lung injury. Am J Physiol Lung Cell Mol Physiol 2017;312:L297–308.

[42] Sammani S, Moreno-Vinasco L, Mirzapoiazova T, Singleton PA, Chiang ET, Evenoski CL, et al. Differential effects of sphingosine 1-phosphate receptors on airway and vascular barrier function in the murine lung. Am J Respir Cell Mol Biol 2010;43:394–402.

[43] Haserodt S, Aytekin M, Dweik RA. A comparison of the sensitivity, specificity, and molecular weight accuracy of three different commercially available hyaluronan ELISA-like assays. Glycobiology 2011;21:175–83.

[44] Piccioni F, Malvicini M, Garcia MG, Rodriguez A, Atorrasagasti C, Kippes N, et al. Antitumor effects of hyaluronic acid inhibitor 4-methylumbelliferone in an orthotopic hepatocellular carcinoma model in mice. Glycobiology 2012;22:400–10.

[45] Sukowati CHC, Anfuso B, Fiore E, Ie SI, Raseni A, Vascotto F, et al. Hyaluronic acid inhibition by 4-methylumbelliferone reduces the expression of cancer stem cells markers during hepatocarcinogenesis. Sci Rep 2019;9:4026.

[46] Bradvik I, Wollmer P, Evander E, Larusdottir H, Blom-Bulow B, Jonson B. Kinetics of lung clearance of 99mTc-DTPA in smoking patients with sarcoidosis compared to healthy smokers. Respir Med 2002;96:317–21.

[47] Grosser OS, Ruf J, Kupitz D, Pethe A, Ulrich G, Genseke P, et al. Pharmacokinetics of 99mTc-MAA- and 99mTc-HSA-microspheres used in preradioembolization dosimetry: influence on the liver-lung shunt. J Nucl Med 2016;57:925–7.

[48] Liu Z, Chen L, Liu S, Barber C, Stevenson GD, Furenlid LR, et al. Kinetic characterization of a novel cationic (99m)Tc(I)-tricarbonyl complex, (99m)Tc-15C5-PNP, for myocardial perfusion imaging. J Nucl Cardiol 2010;17:858–67.

[49] Lee N, Chan MC, Lui GC, Li R, Wong RY, Yung IM, et al. High viral load and respiratory failure in adults hospitalized for respiratory syncytial virus infections. J Infect Dis 2015;212:1237–40.

[50] Duncan CB, Walsh EE, Peterson DR, Lee FE, Falsey AR. Risk factors for respiratory failure associated with respiratory syncytial virus infection in adults. J Infect Dis 2009;200:1242–6.

[51] Jiang D, Liang J, Noble PW. Hyaluronan as an immune regulator in human diseases. Physiol Rev 2011;91:221–64.

[52] Marini JJ, Gattinoni L. Management of COVID-19 respiratory distress. JAMA 2020;323:2329–30.

[53] Coradini D, Zorzet S, Rossin R, Scarlata I, Pellizzaro C, Turrin C, et al. Inhibition of hepatocellular carcinomas in vitro and hepatic metastases in vivo in mice by the histone deacetylase inhibitor HA-but. Clin Cancer Res 2004;10:4822–30.

[54] Monslow J, Sato N, Mack JA, Maytin EV. Wounding-induced synthesis of hyaluronic acid in organotypic epidermal cultures requires the release of heparin-binding egf and activation of the EGFR. J Invest Dermatol 2009;129:2046–58.

[55] Mack JA, Abramson SR, Ben Y, Coffin JC, Rothrock JK, Maytin EV, et al. Hoxb13 knockout adult skin exhibits high levels of hyaluronan and enhanced wound healing. FASEB J 2003;17:1352–4.

[56] Tammi R, Pasonen-Seppanen S, Kolehmainen E, Tammi M. Hyaluronan synthase induction and hyaluronan accumulation in mouse epidermis following skin injury. J Invest Dermatol 2005;124:898–905.

[57] Ghazi K, Deng-Pichon U, Warnet JM, Rat P. Hyaluronan fragments improve wound healing on in vitro cutaneous model through P2X7 purinoreceptor basal activation: role of molecular weight. PLoS One 2012;7:e48351.

[58] Chen WY, Abatangelo G. Functions of hyaluronan in wound repair. Wound Repair Regen 1999;7:79–89.

[59] Kim Y, Kessler SP, Obery DR, Homer CR, McDonald C, de la Motte CA. Hyaluronan 35kDa treatment protects mice from Citrobacter rodentium infection and induces epithelial tight junction protein ZO-1 in vivo. Matrix Biol 2017;62:28–39.

[60] Saikia P, Roychowdhury S, Bellos D, Pollard KA, McMullen MR, McCullough RL, et al. Hyaluronic acid 35 normalizes TLR4 signaling in Kupffer cells from ethanol-fed rats via regulation of microRNA291b and its target Tollip. Sci Rep 2017;7:15671.

[61] Kim Y, West GA, Ray G, Kessler SP, Petrey AC, Fiocchi C, et al. Layilin is critical for mediating hyaluronan 35kDa-induced intestinal epithelial tight junction protein ZO-1 in vitro and in vivo. Matrix Biol 2018;66:93–109.

[62] Saikia P, Bellos D, McMullen MR, Pollard KA, de la Motte C, Nagy LE. MicroRNA 181b–3p and its target importin alpha5 regulate toll-like receptor 4 signaling in Kupffer cells and liver injury in mice in response to ethanol. Hepatology 2017;66:602–15.

[63] Matthay MA, Aldrich JM, Gotts JE. Treatment for severe acute respiratory distress syndrome from COVID-19. Lancet Respir Med 2020;8:433–4.

[64] Black KE, Collins SL, Hagan RS, Hamblin MJ, Chan-Li Y, Hallowell RW, et al. Hyaluronan fragments induce IFNbeta via a novel TLR4-TRIF-TBK1-IRF3-dependent pathway. J Inflamm 2013;10:23 (Lond).

[65] Scheibner KA, Lutz MA, Boodoo S, Fenton MJ, Powell JD, Horton MR. Hyaluronan fragments act as an endogenous danger signal by engaging TLR2. J Immunol 2006;177:1272–81.

[66] Jiang D, Liang J, Fan J, Yu S, Chen S, Luo Y, et al. Regulation of lung injury and repair by toll-like receptors and hyaluronan. Nat Med 2005;11:1173–9.

[67] Modig J, Hallgren R. Increased hyaluronic acid production in lung–a possible important factor in interstitial and alveolar edema during general anesthesia and in adult respiratory distress syndrome. Resuscitation 1989;17:223–31.

[68] Rojas M, Woods CR, Mora AL, Xu J, Brigham KL. Endotoxin-induced lung injury in mice: structural, functional, and biochemical responses. Am J Physiol Lung Cell Mol Physiol 2005;288:L333–41.

[69] Louderbough JM, Lopez JI, Schroeder JA. Matrix hyaluronan alters epidermal growth factor receptor-dependent cell morphology. Cell Adh Migr 2010;4:26–31.

[70] Ni K, Gill A, Tseng V, Mikosz AM, Koike K, Beatman EL, et al. Rapid clearance of heavy chain-modified hyaluronan during resolving acute lung injury. Respir Res 2018;19:107.

[71] Scott JE, Cummings C, Brass A, Chen Y. Secondary and tertiary structures of hyaluronan in aqueous solution, investigated by rotary shadowing-electron microscopy and computer simulation. Hyaluronan is a very efficient network-forming polymer. Biochem J 1991;274(Pt 3):699–705.

[72] Cantor JO. Potential therapeutic applications of hyaluronan in the lung. Int J Chron Obstruct Pulmon Dis 2007;2:283–8.

[73] Fialho de Araujo A, Oliveira-Filho RM, Trezena AG, Borelli P, Mathison R, Tavares de Lima W. Role of submandibular salivary glands in LPS-induced lung inflammation in rats. Neuroimmunomodulation 2002;10:73–9.

[74] Lomniczi A, Mohn C, Faletti A, Franchi A, McCann SM, Rettori V, et al. Inhibition of salivary secretion by lipopolysaccharide: possible role of prostaglandins. Am J Physiol Endocrinol Metab 2001;281:E405–11.

[75] Fernandez-Solari J, Prestifilippo JP, Ossola CA, Rettori V, Elverdin JC. Participation of the endocannabinoid system in lipopolysaccharide-induced inhibition of salivary secretion. Arch Oral Biol 2010;55:583–90.